Asian Journal of Chemistry; Vol. 36, No. 7 (2024), 1641-1649

ASIAN JOURNAL OF CHEMISTRY

https://doi.org/10.14233/ajchem.2024.31733

Combustion Synthesis and Study of Crystallographic and Luminescence Aspects of Double Perovskite $Ba_2BiYO_6:Sm^{3+}$ Nanocrystal for Modern Lighting Applications

OJAS GARG[1], MUKESH KUMAR[2], HINA DALAL[3], POONAM DEVI[3], NEERAJ SEHRAWAT[3], DIKSHA SOLANKI[3] and SUNITA DAHIYA[1,*]

[1]Department of Physics, Baba Mastnath University, Rohtak-124001, India
[2]Department of Chemistry, Vaish College, Rohtak-124001, India
[3]Department of Chemistry, Maharshi Dayanand University, Rohtak-124001, India

*Corresponding author: E-mail: sunitadahiya2311@gmail.com

Received: 12 April 2024; *Accepted*: 1 June 2024; *Published online*: 29 June 2024; AJC-21684

A Sm^{3+}-activated double perovskite Ba_2BiYO_6 nanocrystal system exhibiting a strong orange-red luminescence was prepared using an energy-efficient solution combustion synthetic procedure. The crystal structures were found to be cubic and belong to the $Fm\bar{3}m$ (225) space group with irregular shapes having a mean diameter of 51 nm. The surface aspects were explored *via* scanning and transmission electron microscopic (SEM and TEM) techniques. After exposure to UV energy (410 nm), the nanocrystals emit a active reddish-orange light at 16447 cm^{-1}, caused by the transition from the $^4G_{5/2} \rightarrow {}^6H_{7/2}$ electronic state. The effects of energy transfer were also considered. The highest photoluminescence emission intensity occurs at a concentration of 3.0 mol% Sm^{3+} ions after which starts declining owing to the formation of *d-d* interactions of concentration quenching. The colour coordinates, based on the chromaticity chart, fall within the reddish region and the correlated colour temperature (CCT) value was measured at 1715 K for optimal sample $Ba_2BiY_{0.97}Sm_{0.03}O_6$. Consequently, these nanocrystals are well-suited for use in white lighting emitting (WLED) manufacturing and designed primarily for the purpose of constructing attractive modern lighting components.

Keywords: Nanocrystal, Double perovskite, Photoluminescence, Concentration quenching, Modern lighting.

INTRODUCTION

Several researchers are working in the materials field have made significant contributions to electronic devices and solid-state illumination (SSI) with particular emphasis on the large group of rare-earth doped nanophosphors. Compared with traditional light bulbs, white light emitting diodes (WLEDs) have numerous rewards, like energy efficiency, long service life, minimum mercury content, upgraded robustness and eco-friendliness [1,2]. Rare-earth ions have attractive properties that make them useful in the field of optics. These include good fluorescence capabilities in the visible spectrum, rich energy, high quantum yields and significant emission cross-sections. The arrangement of dopant ions in the host matrix significantly affects the optoelectronic properties [3,4]. Therefore, it is important to choose the right host matrix that meets the requirements.

Yttrium-based matrix media has good photonic properties and structural steadiness and serves as a crucial host matrix [5-8]. In this case, the authors fabricated a series of stable and thermally efficient orange-red emitting Sm^{3+}-activated yttrium-based Ba_2BiYO_6 nanocrystals that can be used as complementary components for free LED lights. No crystallographic and photometric data on the orange emission of nanophosphor systems have been found in previous studies. The stability of the prepared nanophosphors was improved by calcination at 900 ºC for a time span of 3 h.

Various wet methods such as hydrothermal, solvothermal, sol-gel and microwave synthesis have been proposed to obtain good nanomaterials [9,10]. Currently, the solution combustion (SC) method is recognized as a phosphor synthesis method that produces uniform, single-phase, high-purity and large-size crystals over a wide area [11,12]. In recent fabrication, urea serves as a fuel and reducer, whereas metal nitrates serve as oxidants. Several characterizations were performed on the nanocrystalline powder. The Rietveld refinement *via* the X-ray diffraction (XRD) analysis confirmed the formation of cubic phase nanocrystals while the size and surface aspects were analyzed

by TEM and SEM techniques. Photoluminescence (PL) spectra show strong orange-red emission, which is confirmed by the colorimetric (CIE) and associated colour temperature.

EXPERIMENTAL

Nanomaterial synthesis: An economical and low-temperature SC synthetic method was adopted to fabricate nanosamples with controlled chemical reactions. This method uses $Bi(NO_3)_3 \cdot 6H_2O$, $Y(NO_3)_3$, $Sm(NO_3)_3$, $Ba(NO_3)_2$ and urea. The very first part of the synthetic procedure involves the mixing of the raw materials in a small quantity of H_2O then warmed at a hot plate and thereafter put in the furnace for combustion in which several gases evolved and a solid, crispy and fluffy powder separates out [13,14] which was then calcined at 900 ºC for 3 h to increase the luminescencity. The morphology of the prepared nanosamples may be controlled using the SC method. The calcined powder was allowed to cool to room temperature before being pulverized and refined using a mortar to enhance its varied properties. The procedure can be represented through chemical reactions as follows:

$$2Ba(NO_3)_2 \cdot 4H_2O + Bi(NO_3)_3 \cdot 6H_2O + (1-x)Y(NO_3)_3 \cdot 6H_2O + xSm(NO_3)_3 \cdot 6H_2O + NH_2CONH_2 \rightarrow Ba_2BiY_{(1-x)}Sm_xO_6 + N_2(g) + H_2O(g) + CO_2(g)$$

A general flow diagram consisting of the SC synthetic procedure is represented in Fig. 1.

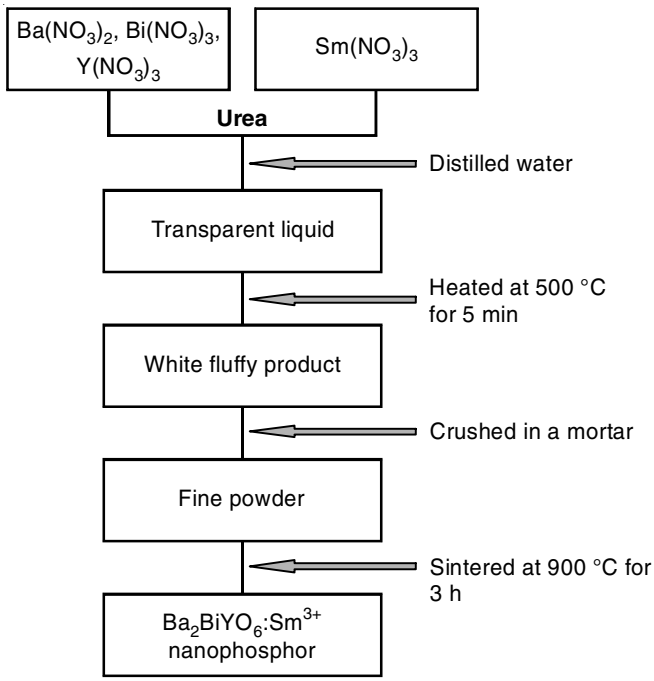

Fig. 1. A schematic flow diagram for the fabrication of Sm^{3+}-activated Ba_2BiYO_6 nanophosphor

Characterization: The phase analysis of the synthesized nanoparticles was performed using advanced equipment Rigaku Ultima IV, a sophisticated diffractometer from Japan. Furthermore, the nanoparticles were examined by conducting PXRD measurements. The measurements involve 2º/min scanning speed with an angle ranging from 10 to 80º. The PXRD setup employed Cu*K*α radiation, λ = 0.15405 nm, TC (tube current) = 40 mA and TV (tube voltage) = 40 kV. To refine the background, modified Chebyshev's three terms *via* the general structural analysis system (GSAS) platform [15,16]. For analyzing the size and shape of the crystals, the T20 S TWIN FEI TEM and SEM (JSM-6510 JEOL) instruments have been utilized. The EDAX system (AMETEK) measures the quantity of constituents present in the nanosamples. To investigate the durability, colour characteristics and optical assets, the Xe lamp Hitachi F 7000 spectrophotometer was employed, which captured both the excitation and emission spectra. The specific parameters employed were a 700 nm PMT voltage and a 5 mm of slit width. In addition to the above-mentioned instruments and techniques, the host matrix and doped nanosample band gaps were explored using diffuse reflectance (DR) spectroscopic analysis.

RESULTS AND DISCUSSION

Crystal structure measurements: The crystal structure was investigated by means of powder X-ray diffraction (PXRD) analysis, which showed that the doped samples' PXRD patterns match with the unique pattern associated with CIF # 2002487 (Fig. 2). Furthermore, the doped optimal sample underwent refinement through the Rietveld progression to authenticate the development of cubic crystals of nanosize. A comparison was conducted between the unit cell size of the pure host matrix and the doped nanocrystals. The results (Table-1) showed the minimal variations in the crystal limits, suggesting a similarity between the Ba_2BiYO_6 host matrix and doped $Ba_2BiY_{0.97}Sm_{0.03}O_6$ configuration.

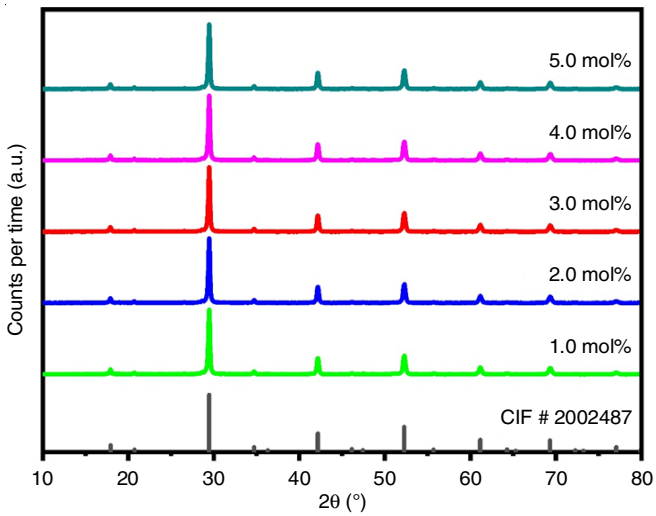

Fig. 2. Collective powder XRD outlines of $Ba_2BiY_{(1-x)}O_6$:xSm^{3+} (x = 0.01-0.05) nanophosphor showing complete alliance with the standard host patterns

Post-refinement, the cell constraints for the optimal sample were determined as follows: $a = b = c = 8.5762$ Å, cell volume = 631.57 Å^3, Z = 4 and $\alpha = \beta = \gamma = 90°$. The consequences of the Rietveld procedure before and after doping are shown in Figs. 3a and 3b, along with the values of $\chi^2 = 2.714$, R_p = 7.23% and wR_p = 8.67% for the latter. Additional refined constraints can be found in Table-2.

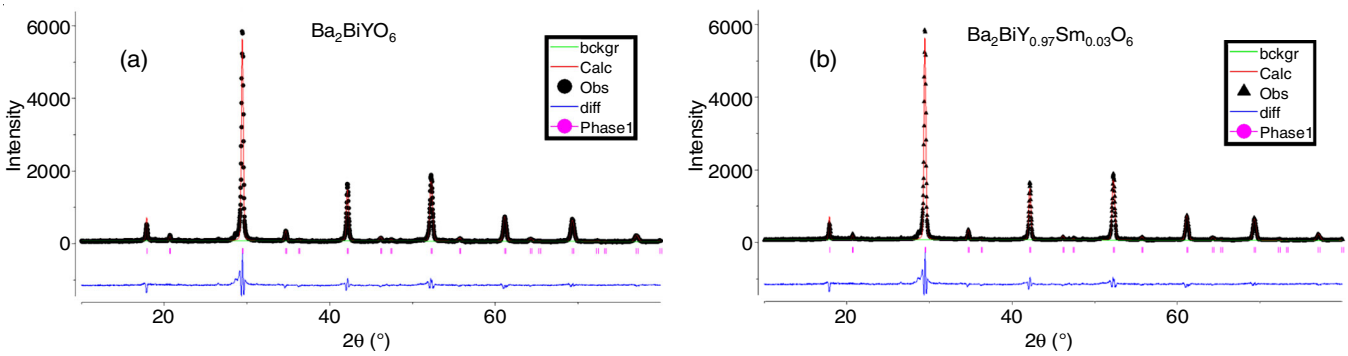

Fig. 3. (a) Rietveld refinement results performed over the host matrix Ba_2BiYO_6 to confirm the cubic phase formed with values of refined parameters as wR_P (Goodness of fit) = 8.62 %, R_P (Residual of least squares) = 7.51% and $\chi^2 = 2.328$; (b) Rietveld refinement results performed over the optimized nano sample $Ba_2BiY_{0.97}Sm_{0.03}O_6$ yielding refined parameters of wR_P (Goodness of fit) = 8.75 %, R_P (Residual of least squares) = 7.66% and $\chi^2 = 2.347$

TABLE-1
COMPARATIVE STUDIES OF CRYSTAL STRUCTURE PARAMETERS OF PURE HOST MATRIX Ba_2BiYO_6 AND OPTIMIZED NANOPHOSPHOR $Ba_2BiY_{0.97}Sm_{0.03}O_6$

Formula	Ba_2BiYO_6	$Ba_2BiY_{0.97}Sm_{0.03}O_6$
Formula type	ABC2X6	ABC2X6
Symmetry	Cubic	Cubic
Space group	$Fm\ \bar{3}m$ (225)	$Fm\ \bar{3}m$ (225)
a = b = c (Å)	8.5681(17)	8.5762(17)
Z	4	4
α = β = γ (degree)	90	90
Volume of cell (Å^3)	629.00(37)	631.57(400)
Density (g cm^{-3})	7.0572	6.9952
Pearson code	cF40	cF40
Wyckoff sequence	ecba	ecba

It was observed that the substitution of smaller Y^{3+} ions with slightly larger Sm^{3+} ions led to a tiny increase in cell volume. This observation is supported by the equation:

$$\Delta_r = \frac{R_m(CN) - R_d(CN)}{R_m(CN)} \times 100 \quad (1)$$

where CN is the coordination number, while R_m (CN) and R_d (CN) represent the ionic dimensions of Ba_2BiYO_6 host and Sm^{3+} doped cations, respectively. The ionic extents of Y^{3+} and Sm^{3+} ions are 0.90 and 0.95 Å and hence the Δ_r parameter for the same was determined to be 5.26%. This value which is pretty below 30% and similar charges align with viable replacements [17]. Additionally, the same charge causes the transfer of these ions.

The crystal prototype of the optimal nanocrystalline powder was determined using the Diamond 4.5.2 program. Fig. 4 depicts the general interpretation of the unit cell, exhibiting various coordination environments around discrete atoms in which 'Ba' atoms form the 12-coordinated geometry and 'O' atoms generate octahedra around Bi and Y/Sm atoms.

Furthermore, the mean dimension of the prepared nanocrystals were calculated using Scherrer's formula [18,19]:

$$D = \frac{0.941\lambda}{\beta\cos\theta} \quad (2)$$

where D represents the average crystal size, λ represents the X-ray wavelength used (0.1540 nm), β represents the FWHM and θ represents the diffraction angle. The 'D' has been found to possess a value of 51 nm.

Morphological characteristics: The texture and extent of the prepared nanocrystals significantly influence their luminescent properties. The SEM image in Fig. 5a reveals a distinct combination of nanoparticles with varying morphologies. Furthermore, the presence of holes and cracks suggests the occurrence of an SC procedure [20]. The TEM image (Fig. 5b) also confirmed the size range of the fabricated nanocrystals, which falls in the nano range and is reliable with the value obtained from Scherrer's equation (51 nm). The EDAX maps and spectra (Fig. 6a and 6b) confirmed the occurrence of the bulk substance in the synthesized samples and verified the successful accumulation of Sm^{3+} ions into the Ba_2BiYO_6 host matrix.

Energy band gap: The UV-DR spectra (200-800 nm) of Ba_2BiYO_6 and $Ba_2BiY_{0.97}Sm_{0.03}O_6$ were analyzed to regulate the energy difference. The Tauc plot of the Kubelka–Munk function was applied to estimate both direct and indirect band gap transitions of nanoscaled materials. The Kubelka–Munk function relation can be expressed as [18]:

$$F(R_\infty) = \frac{(1-R_\infty)^2}{2R_\infty} = \frac{K}{S} \quad (3)$$

TABLE-2
VARIOUS REFINED ATOMIC PARAMETERS AND OCCUPANCIES OF SEVERAL ELEMENTS PRESENT IN $Ba_2BiY_{0.97}Sm_{0.03}O_6$ NANOSAMPLE

Atom	Ion type	Wyck.	Site	Occupancy	x/a	y/b	z/c
Ba1	Ba^{2+}	8c	-43m	1.00	1/4	1/4	1/4
Bi1	Bi^{3+}	4a	m-3m	1.00	0	0	0
Y1	Y^{3+}	4b	m-3m	0.97	1/2	0	0
Sm1	Sm^{3+}	4b	m-3m	0.03	1/2	0	0
O1	O^{2-}	24e	4m.m	1.00	0.246	0	0

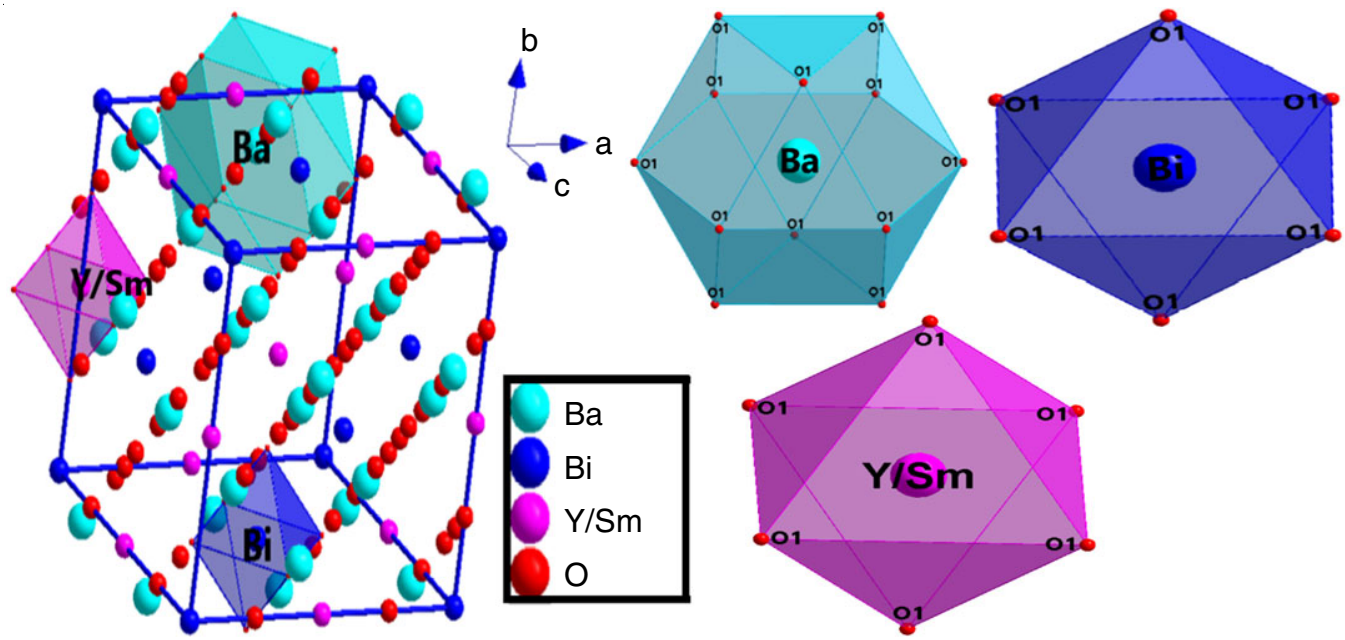

Fig. 4. The crystal structure of the fabricated Sm^{3+} doped Ba_2BiYO_6 nanophosphor and coordination spheres of different types of atoms present

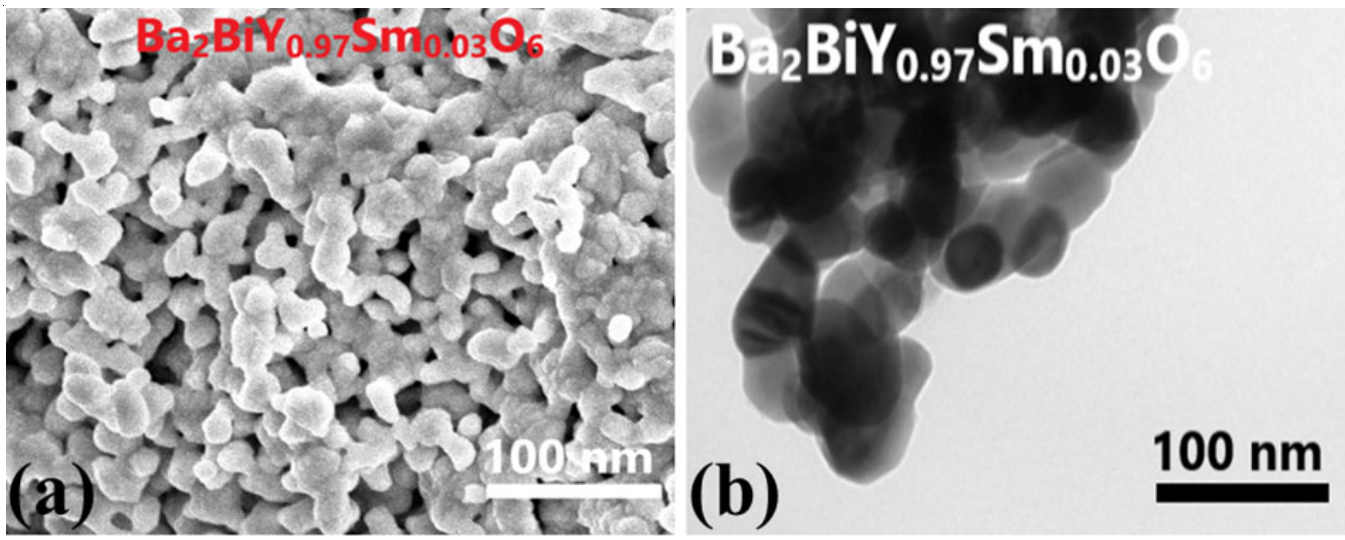

Fig. 5. (a) SEM and (b) TEM micrographs of $Ba_2BiY_{0.97}Sm_{0.03}O_6$ nanophosphor representing the surface features at a sintering temperature of 900 °C

$$h\nu = \frac{1240}{\lambda} \quad (4)$$

where $F(R_\infty)$ represents the Kubelka-Munk function; K and S represent the absorption and scattering coefficients, hν represents the energy of a photon and λ is the wavelength used. Based on this approach, the E_g (band gap) was determined using eqn. 5:

$$[F(R_\infty)h\nu]^n = C(h\nu - E_g) \quad (5)$$

where, C is a constant term and the value of "n" is fixed at 0.5 for indirect acceptable, 1.5 for direct repressed, 2 for direct acceptable and 3 for indirect repressed electronic transitions. Plotting the tangent of the *x*-axis between $(\alpha h\nu)^2$ and hν for both the host base material and the optimized nanocrystals provided the E_g values (Fig. 7a-b) in which the E_g of the latter was measured to be 2.15 eV, while the former had a value of 2.05 eV. The smaller bandgap in the latter case is owing to the presence of supplementary energy levels in the made-up nanocrystals, which contribute to efficient light emission. These energy bandgap values demonstrate favourable compatibility with wide band-gap semiconducting materials, indicating their potential use in military radars, laser technology and pc-wLEDs.

Luminescence properties: Fig. 8a portrays the excitation outline of the $Ba_2BiY_{0.93}Sm_{0.03}O_6$ (optimal nanosample) which consists of distinct excitations at 348, 366, 383, 410, 424, 472 and 484 nm owing to electronic transitions from $^6H_{5/2}$ to $^4D_{7/2}$, $^4F_{9/2}$, $^4D_{5/2}$, $^4K_{11/2}$, $^6P_{5/2} + {}^4M_{19/2}$, $^4F_{5/2} + {}^4I_{13/2}$ and $^4G_{7/2}$ states, respectively [21-24] out of which the band at 410 nm appears

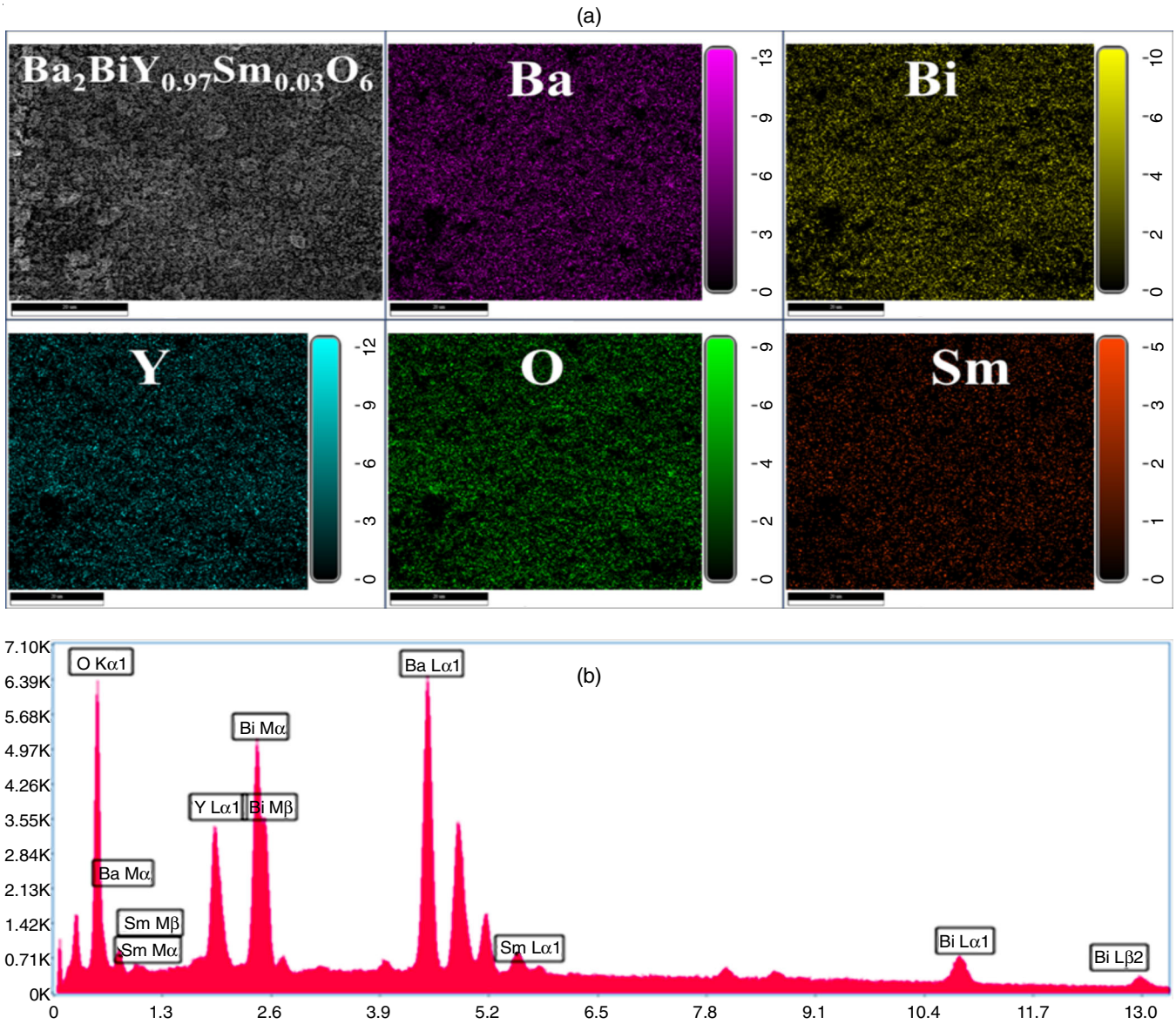

Fig. 6. (a) Energy dispersive maps of all elements present in optimized doped nanophosphor $Ba_2BiY_{0.97}Sm_{0.03}O_6$ in a field of view of the spectrum; (b) EDAX analysis of optimal nanophosphor $Ba_2BiY_{0.97}Sm_{0.3}O_6$ showing quantitatively the presence of various elements in the nanophosphor

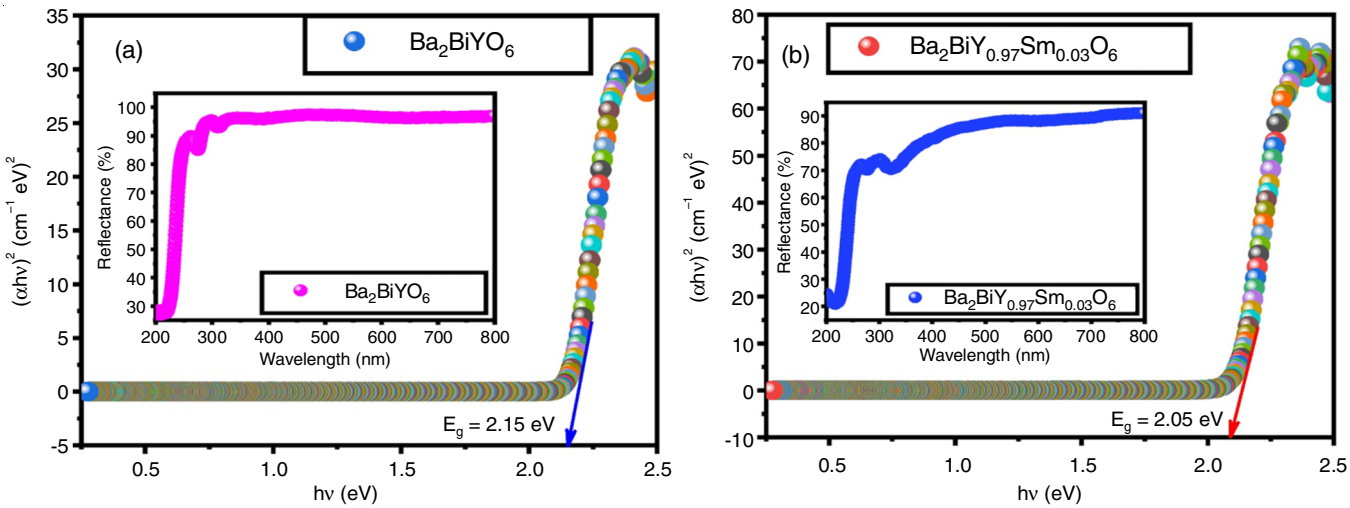

Fig. 7. Tauc's plot to determine energy band-gap (E_g) for (a) the host matrix Ba_2BiYO_6 and (b) the optimized nanophosphor $Ba_2BiY_{0.97}Sm_{0.03}O_6$

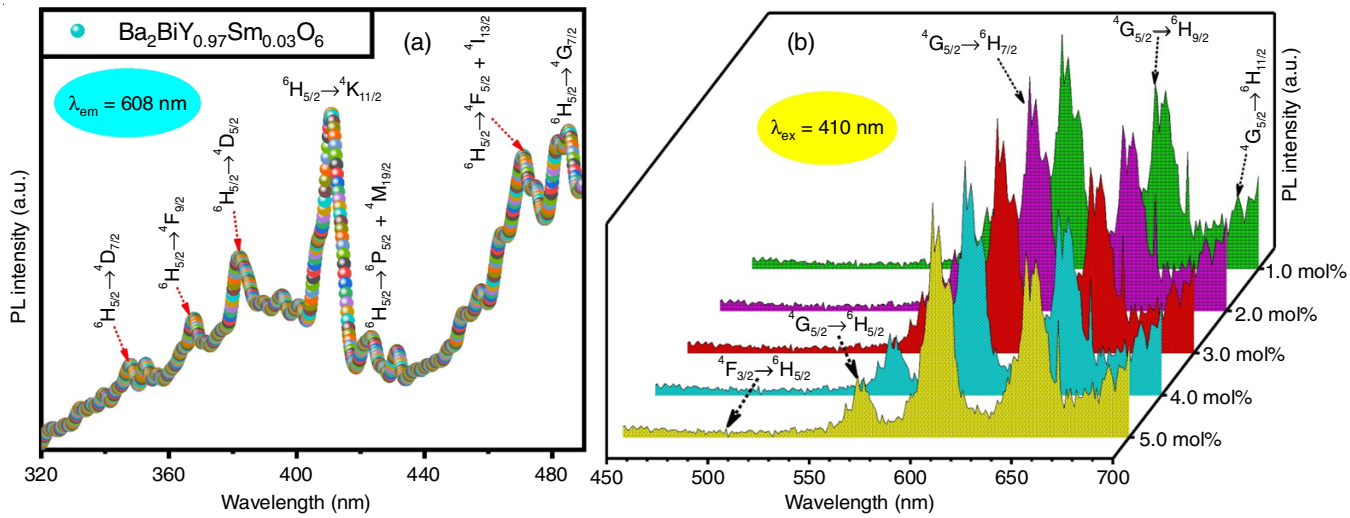

Fig. 8. Photoluminescence excitation spectrum of (a) $Ba_2BiY_{0.97}Sm_{0.03}O_6$ nanophosphor recorded at λ_{em} = 608 nm and (b) $Ba_2BiY_{(1-x)}O_6:xSm^{3+}$ (x = 0.01-0.05) nanophosphor recorded at λ_{ex} = 410 nm

the most intense. After changing the composition of Sm^{3+} ions, the overall process and the exact position of the electronic transition in the spectrum remain unchanged [25,26]. Then, the emission spectrum at a wavelength of 410 nm was recorded in the range of 450-700 nm (Fig. 8b) which comprises maxima at 525 nm ($^4F_{3/2}\rightarrow{}^6H_{5/2}$), 565 nm ($^4G_{5/2}\rightarrow{}^6H_{5/2}$), 608 nm ($^4G_{5/2}\rightarrow{}^6H_{7/2}$), 667 nm ($^4G_{5/2}\rightarrow{}^6H_{9/2}$) and 692 nm ($^5D_3\rightarrow{}^6H_{11/2}$) [27,28].

Fig. 9a illustrates the discrete electronic transformations with their equivalent wavenumbers and energy levels. The relative intensities of these transitions can be found in Table-3, along with the comparative photoluminescence (PL) strength for each conversion. Moreover, the dependence of the energy on the dopant composition is shown in Fig. 9b. It should be noted that initially, the PL power surges up to a concentration of 3.0 mol% of Sm^{3+} ions, but then begins to decrease. This decline is attributed to the concentration quenching parameter, which refers to the loss of radiative energy. Several factors, such as radiation reabsorption, other exchanges and multipolar interactions, can contribute to this phenomenon.

There is no overlap in the PL patterns, indicating that the chance of energy reabsorption is very small. The R_c, the critical distance has an important role in determining how energy is exchanged between activator particles, which occurs only when the distance is less than or equal to 4 Å. In such cases, Blasse's formulation is useful [29]:

$$R_c = 2\left(\frac{3V}{4\pi x_c N}\right)^{1/3} \quad (6)$$

In this case, x represents the dopant amount (in mol%) that yields the highest PL intensity, V represents the volume of the unit cell and N characterizes the numeral value of cations in a unit cell. Given these conditions, R_c was found to be 10.79 Å, which significantly exceeds the permissible critical distance (5 Å) for carrying out the exchange procedure. Therefore, the potential mechanisms causing concentration quenching are likely to involve *d-d*, *d-q* or *q-q* interactions. To determine the specific type of exchange, the Dexter's formula [30] was applied:

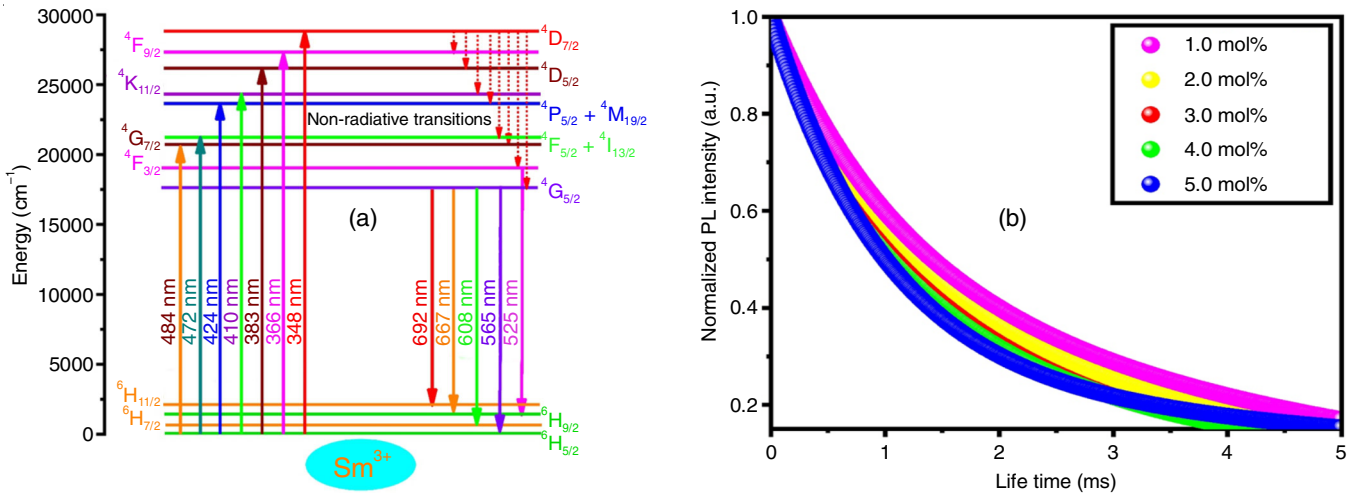

Fig. 9. (a) Descriptive energy level diagram displaying distinct electronic transitions with the corresponding wavelength in diverse energy levels for the Sm^{3+} - doped Ba_2BiYO_6 nanophosphor; (b) Lifetime decay curves of $Ba_2BiY_{(1-x)}O_6:xSm^{3+}$ (x = 0.01-0.05) nanophosphor system recorded at λ_{ex} = 410 nm and λ_{em} = 608 nm

TABLE-3
TYPES OF ELECTRONIC TRANSITIONS OCCURRING IN THE SPECTRA OF Sm^{3+} - DOPED Ba_2BiYO_6 NANOPHOSPHORS, THEIR POSITIONS AND RELATIVE INTENSITIES

Nanophosphor	Kind of spectrum	Transitions	Wavenumber (cm^{-1})	Intensity
$Ba_2BiY_{(1-x)}Sm_xO_6$	Excitation at λ_{em} = 608 nm	$^6H_{5/2} \rightarrow {}^4D_{7/2}$	28735	Weak
		$^6H_{5/2} \rightarrow {}^4F_{9/2}$	27322	Weak
		$^6H_{5/2} \rightarrow {}^4D_{5/2}$	26109	Medium
		$^6H_{5/2} \rightarrow {}^4K_{11/2}$	24390	Very strong
		$^6H_{5/2} \rightarrow {}^6P_{5/2}+{}^4M_{19/2}$	23585	Weak
		$^6H_{5/2} \rightarrow {}^4F_{5/2}+{}^4I_{13/2}$	21186	Strong
		$^6H_{5/2} \rightarrow {}^4G_{7/2}$	20661	Strong
	Emission at λ_{ex} = 410 nm	$^4F_{3/2} \rightarrow {}^6H_{5/2}$	19047	Weak
		$^4G_{5/2} \rightarrow {}^6H_{5/2}$	17699	Medium
		$^4G_{5/2} \rightarrow {}^6H_{7/2}$	16447	Very strong
		$^4G_{5/2} \rightarrow {}^6H_{9/2}$	14992	Strong
		$^4G_{5/2} \rightarrow {}^6H_{11/2}$	14451	Medium

$$\log\left(\frac{I}{x}\right) = -\frac{s}{d}\log(x) + \log(f) \quad (7)$$

where I/x represents the segment of Sm^{3+} ions emission intensity and the composition. Meanwhile, d represents the size of the sample, specifically '3' in this case. Additionally, x denotes the Sm^{3+} composition exceeding the optimum value. Moreover, 's' characterizes a constant term encompassing energy communication values for qq, dq and dd, which are 10, 8 and 6, respectively. The graph of log(I/x) against log(x) (Fig. 10) exhibits a linear relationship with a slope value of -1.7305 ± 0.0043, corresponding to s = 5.1915 ≈ 6. This finding confirms the involvement of *d-d* exchanges in concentration quenching.

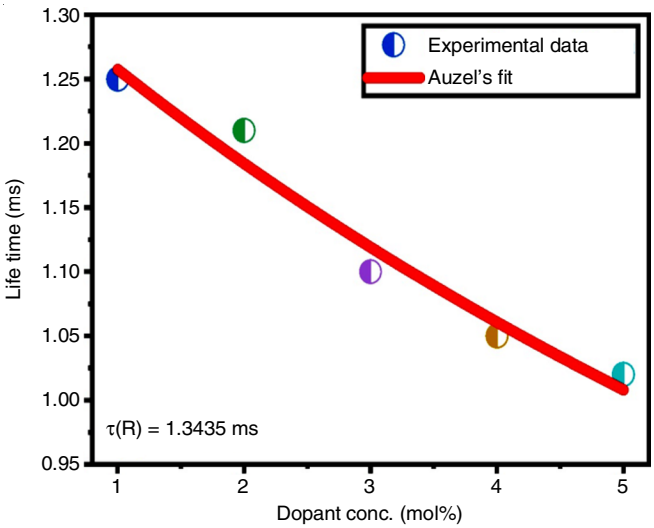

Fig. 10. Effect of Sm^{3+} composition (1.0-5.0 mol%) on decay lifetime of Ba_2BiYO_6 nanophosphor *via* Auzel's formulation

The luminescence decay curves, illustrated in Fig. 11, were obtained by exciting the nanophosphor at 410 nm and measuring the emission wavelength at 608 nm. The mono-exponential performance is exhibited by the decay curves as described by eqn. 8:

$$I = I_0 \exp\left(\frac{-t}{\tau}\right) \quad (8)$$

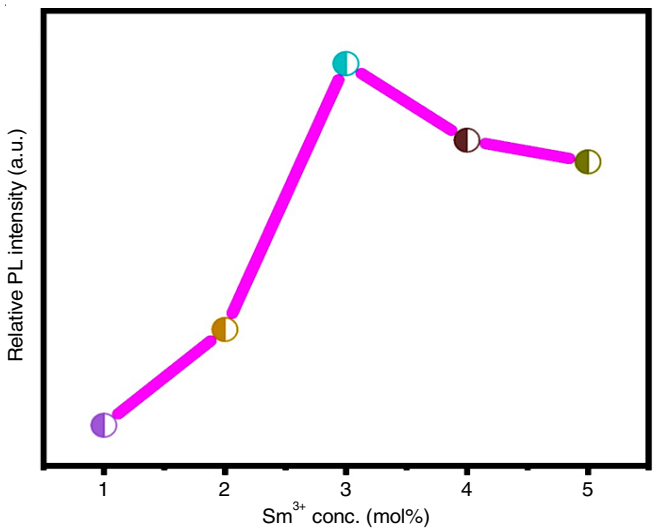

Fig. 11. Interdependence of the PL intensity and composition of the Sm^{3+} - doped Ba_2BiYO_6 (1.0-5.0 mol%) nanophosphor

The I and I_o values represent the PL strength at t = 0 and t = t, respectively. The quantum efficiency, lifetime decay and rates of radiation-less transitions are determined and shown in Table-4.

TABLE-4
PHOTOLUMINESCENCE LIFETIME, QUANTUM EFFICIENCY AND RATES OF NON-RADIATIVE TRANSITIONS FOR $Ba_2BiY_{(1-x)}O_6:xSm^{3+}$ (x = 0.01-0.05) NANOPHOSPHOR SYSTEM

Sm^{3+} conc. (mol%)	Lifetime (ms)	Quantum efficiency (%)	Non-radiative rate (s^{-1})
1.0	1.2595	93.74	49.4
2.0	1.2152	90.45	78.6
3.0	1.1605	86.37	117.3
4.0	1.0576	78.71	201.2
5.0	1.0059	74.87	249.8

As the additive composition increases, the lifetime value decreases from 1.2595 ms to 1.0059 ms. The non-radiative relaxation rates of all nanosamples can be calculated using eqn. 9:

$$\frac{1}{\tau_0} = \frac{1}{\tau_R} + A_{nR} \quad (9)$$

The experimental and radiative lifetimes are represented by τ_0 and τ_R, respectively. To calculate τ_R, Auzel's method was utilized (as explained in Fig. 12) [31] in the following manner:

$$\tau(c) = \frac{\tau_R}{1 + \frac{c}{c_0} e^{-N/3}} \quad (10)$$

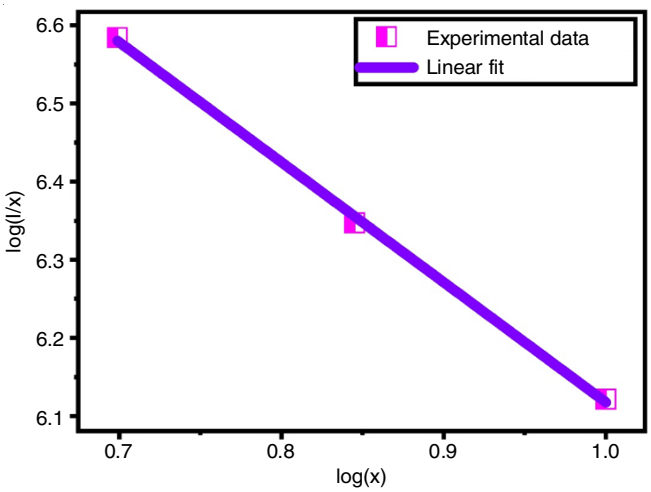

Fig. 12. A linear variation of log(I/x) with log(x) in $Ba_2BiY_{(1-x)}Sm_xO_6$ (x = 3.0-5.0 mol%) nanophosphor to determine the mechanism of concentration quenching phenomenon

In this case, $\tau(c)$ represents the decay lifetime at a particular composition 'c', while N denotes the phonon number and c_0 is a constant specific to the composition. Using this equation, the calculated value of τ_R is 1.3435 ms. Moreover, the quantum efficiency is merely the proportion of the experimental and radiative lifetime.

$$\varphi = \frac{\tau_0}{\tau_R} \quad (11)$$

The quantum efficiency decreases when the Sm^{3+} composition is inclined because the observed lifetime also follows this pattern. This is because energy is transmitted between Sm^{3+} ions *via* a non-radiative mechanism. The optimized sample has a quantum efficiency of 86.37 %.

Colour chromaticity: The nanophosphor's ability to emit light was visually confirmed using the CIE 1931 method. The MATLAB software was used to calculate the colour coordinates of the fabricated samples (Fig. 13a). All the colour coordinates were in the reddish-orange region of the chromaticity map, expanding the potential applications in solid-state lightings, such as pc-WLEDs. Furthermore, the correlated colour temperature (CCT) was evaluated *via* the Mc-Camy simplification as follows [32]:

$$CCT = -437n^3 + 3601n^2 - 6861n + 5514.31 \quad (12)$$

where n represents the proportion of $x\text{-}x_e$ and $y\text{-}y_e$, x and y are the CIE coordinates of the samples and x_e and y_e are the fixed position of the chromaticity epicenter, specifically 0.332 and 0.186, respectively. Additionally, u′ and v′ (CCT coordinates) were calculated according to the eqns. 12 and 14:

$$u' = \frac{4x}{-2x + 12y + 3} \quad (13)$$

$$v' = \frac{9y}{-2x + 12y + 3} \quad (14)$$

The values for u′, v′ coordinates and CIE colour coordinates are shown in Table-5. By calculating the CCT value, it was determined that all the nanosamples are red light emitters and the value for the optimal sample is 1715 K (Fig. 13b), which is much compatible with the manufacturing of WLEDs for the indoor lighting.

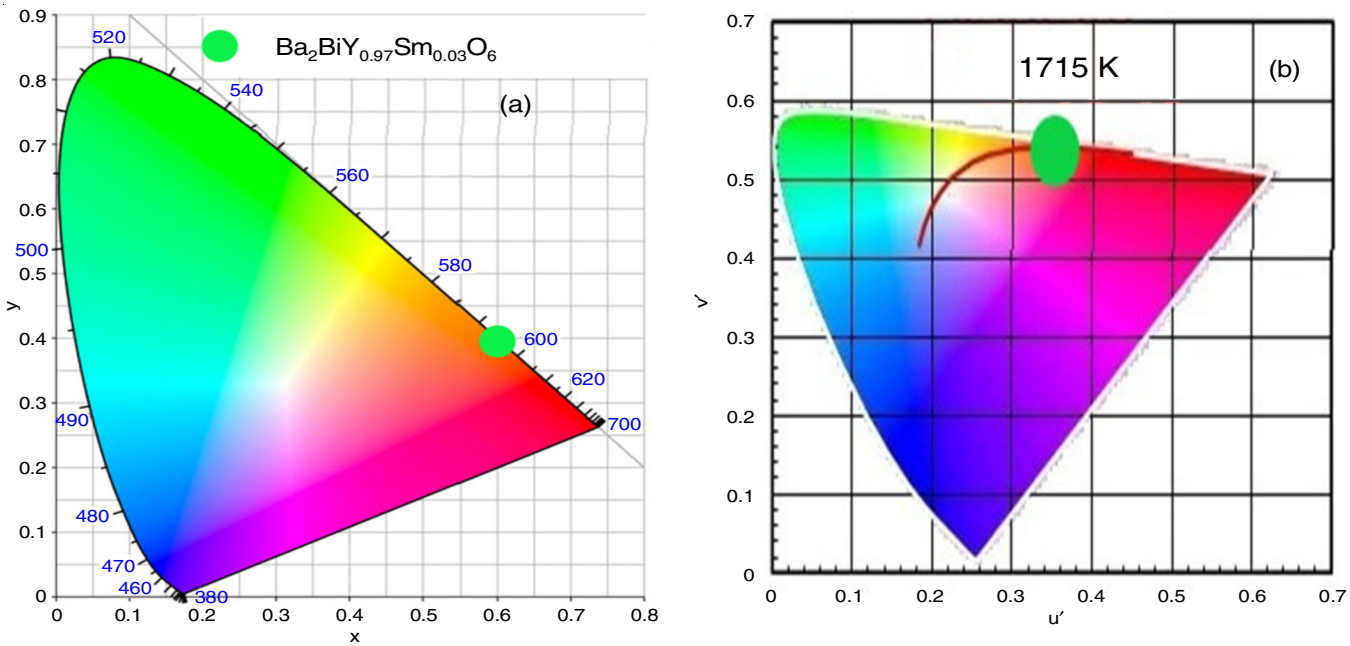

Fig. 13. (a) CIE chromaticity diagram with colour coordinates of the optimized nanophosphor $Ba_2BiY_{0.97}Sm_{0.03}O_6$; (b) CCT coordinates (u′ and v′) with the respective CCT value of the optimal nanophosphor $Ba_2BiY_{0.97}Sm_{0.03}O_6$

TABLE-5
CIE AND CCT COORDINATES ALONG WITH CCT VALUES OF $Ba_2BiY_{(1-x)}O_6:xSm^{3+}$ (x = 0.01-0.05) NANO-CRYSTALLINE PHOSPHORS

$Ba_2BiY_{(1-x)}Sm_xO_6$	CIE coordinates (x, y)	CCT coordinates (u′, v′)	CCT (K)
x = 0.01	0.5875, 0.4022	0.3487, 0.5464	1741
x = 0.02	0.5873, 0.4026	0.3512, 0.5358	1812
x = 0.03	0.5868, 0.4027	0.3524, 0.5442	1715
x = 0.04	0.5870, 0.4036	0.3520, 0.5563	1832
x = 0.05	0.5872, 0.4021	0.3538, 0.5587	1751

Conclusion

The nanocrystals of a cubic structure type with $Fm\bar{3}m$ (225) space group were prepared using a simple solution combustion method. The structure and photoluminescence of nanophosphors were examined in depth by PXRD, EDAX, SEM, TEM, DRS, PL, CIE and CCT analyses. The PXRD results confirmed that the nanoscale structure has a cubic phase. The observations showed that the maximum emission intensity of PL up to the doping concentration of Sm^{3+} ions is 3.0 mol%. After that the intensity gradually decreases owing to the concentration quenching triggered by the *d-d* changes. The quantum efficacy of the optimized structure was 86.37%. Additionally, the optimized nanosample has a lesser band gap energy of 2.15 eV than that of the pure host matrix (2.05 eV), indicating that the doped nanophosphor has good brightness. All the nanosamples exhibit CIE colour coordinates in the reddish-orange region of the chromaticity diagram. The value of the CCT of the optimized sample is 1715 K, expanding its potential use in red light emission for the indoor lighting WLED fabrication.

ACKNOWLEDGEMENTS

The authors are highly thankful to the Department of Physics, Baba Mastnath University, Rohtak, India for providing valuable support and cooperation in every field to carry out this research work.

CONFLICT OF INTEREST

The authors declare that there is no conflict of interests regarding the publication of this article.

REFERENCES

1. P. Pust, V. Weiler, C. Hecht, A. Tücks, A.S. Wochnik, A.-K. Henß, D. Wiechert, C. Scheu, P.J. Schmidt and W. Schnick, *Nat. Mater.*, **13**, 891 (2014); https://doi.org/10.1038/nmat4012
2. M. Liu, W. Lü, J. Huo, B. Shao, Y. Feng, S. Zhao and H. You, *RSC Adv.*, **6**, 92371 (2016); https://doi.org/10.1039/C6RA21254A
3. V. Nazabal and J.-L. Adam, *Optical Mater.: X*, **15**, 100168 (2022); https://doi.org/10.1016/j.omx.2022.100168
4. H. Li, G. Bai, Y. Lian, Y. Li, L. Chen, J. Zhang and S. Xu, *Mater. Design*, **231**, 112036 (2023); https://doi.org/10.1016/j.matdes.2023.112036
5. S. Devi, S. Kaushik, M. Kumar, H. Dalal, S. Gaur and S. Kumar, *Mater. Sci. Eng. B*, **289**, 116273 (2023); https://doi.org/10.1016/j.mseb.2023.116273
6. L. Jing, X. Liu, Y. Li and Y. Wang, *J. Lumin.*, **162**, 185 (2015); https://doi.org/10.1016/j.jlumin.2015.02.048
7. H. Duan, R. Cui, X. Qi and C. Deng, *J. Mol. Struct.*, **1205**, 127551 (2020); https://doi.org/10.1016/j.molstruc.2019.127551
8. J. Dalal, A. Khatkar, M. Dalal, S. Chahar, P. Phogat, V.B. Taxak and S.P. Khatkar, *J. Alloys Compd.*, **821**, 153471 (2020); https://doi.org/10.1016/j.jallcom.2019.153471
9. A. Jain and G.A. Hirata, *Ceram. Int.*, **42**, 6428 (2016); https://doi.org/10.1016/j.ceramint.2016.01.053
10. E. Bonturim, L.G. Merízio, R. dos Reis, H.F. Brito, L.C.V. Rodrigues and M.C.F.C. Felinto, *J. Alloys Compd.*, **732**, 705 (2018); https://doi.org/10.1016/j.jallcom.2017.10.219
11. K.C. Patil, M.S. Hegde, T. Rattan and S.T. Aruna, Chemistry of Nanocrystalline Oxide Materials Combustion Synthesis, Properties and Applications, World Scientific Publishing Co. Pte. Ltd., Singapore (2008).
12. S. Singh, S.P. Khatkar, P. Boora and V.B. Taxak, *J. Mater. Sci.*, **49**, 4773 (2014); https://doi.org/10.1007/s10853-014-8176-5
13. S. Ekambaram and K.C. Patil, *J. Alloys Compd.*, **248**, 7 (1997); https://doi.org/10.1016/S0925-8388(96)02622-9
14. S. Ekambaram and K.C. Patil, *J. Mater. Chem.*, **5**, 905 (1995); https://doi.org/10.1039/jm9950500905
15. P.E. Stutzman and L. Struble, Instructions in Using GSAS Rietveld Software for Quantitative X-Ray Diffraction Analysis of Portland Clinker and Cement (National Institute of Standards and Technology), p. NIST TN 1884 (2015); https://doi.org/10.6028/NIST.TN.1884
16. B.H. Toby, *J. Appl. Cryst.*, **34**, 210 (2001); https://doi.org/10.1107/S0021889801002242
17. M. Dhanalakshmi, H. Nagabhushana, S.C. Sharma, R.B. Basavaraj, G.P. Darshan and D. Kavyashree, *Mater. Res. Bull.*, **102**, 235 (2018); https://doi.org/10.1016/j.materresbull.2018.02.003
18. P. Kubelka, *J. Opt. Soc. Am.*, **38**, 448 (1948); https://doi.org/10.1364/JOSA.38.000448
19. A. Monshi, M.R. Foroughi and M.R. Monshi, *World J. Nano Sci. Eng.*, **2**, 154 (2012); https://doi.org/10.4236/wjnse.2012.23020
20. M.S. Mendhe, S.P. Puppalwar and S.J. Dhoble, *Optik*, **166**, 15 (2018); https://doi.org/10.1016/j.ijleo.2018.04.006
21. J. Xue, M. Song, H.M. Noh, S.H. Park, B.R. Lee, J.H. Kim and J.H. Jeong, *J. Alloys Compd.*, **817**, 152705 (2020); https://doi.org/10.1016/j.jallcom.2019.152705
22. L. Li, X. Tang, Z. Jiang, X. Zhou, S. Jiang, X. Luo, G. Xiang and K. Zhou, *J. Alloys Compd.*, **701**, 515 (2017); https://doi.org/10.1016/j.jallcom.2017.01.171
23. L. Li, S. Fu, Y. Zheng, C. Li, P. Chen, G. Xiang, S. Jiang and X. Zhou, *J. Alloys Compd.*, **738**, 473 (2018); https://doi.org/10.1016/j.jallcom.2017.12.169
24. P. Sehrawat, P. Dayawati, P. Boora, R.K. Malik, S.P. Khatkar and V.B. Taxak, *Ceram. Int.*, **47**, 5432 (2021); https://doi.org/10.1016/j.ceramint.2020.10.125
25. X. Li, Y. Zhang, D. Geng, J. Lian, G. Zhang, Z. Hou and J. Lin, *J. Mater. Chem. C Mater. Opt. Electron. Devices*, **2**, 9924 (2014); https://doi.org/10.1039/C4TC01909A
26. M. Tian, P. Li, Z. Wang, X. Teng, Z. Li, J. Cheng, Y. Sun, C. Wang and Z. Yang, *CrystEngComm*, **18**, 6934 (2016); https://doi.org/10.1039/C6CE01400C
27. P. Sehrawat, R.K. Malik, R. Punia, S.P. Khatkar and V.B. Taxak, *Chem. Phys. Lett.*, **777**, 138743 (2021); https://doi.org/10.1016/j.cplett.2021.138743
28. P. Sehrawat, R.K. Malik, R. Punia, M. Sheoran, N. Kumari, S.P. Khatkar and V.B. Taxak, *J. Mater. Sci. Mater. Electron.*, **32**, 15930 (2021); https://doi.org/10.1007/s10854-021-06144-6
29. G. Blasse, *Phys. Lett. A*, **28**, 444 (1968); https://doi.org/10.1016/0375-9601(68)90486-6
30. H. Dalal, M. Kumar, P. Sehrawat, M. Sheoran, N. Sehrawat, S. Kumar and R.K. Malik, *J. Mater. Sci. Mater. Electron.*, **33**, 13743 (2022); https://doi.org/10.1007/s10854-022-08307-5
31. F. Auzel, *J. Lumin.*, **100**, 125 (2002); https://doi.org/10.1016/S0022-2313(02)00457-X
32. C.S. McCamy, *Color Res. Appl.*, **17**, 142 (1992); https://doi.org/10.1002/col.5080170211